Global Drift Wave Map Test Particle Simulations

J.-M. Kwon[a], W. Horton[b], P. Zhu[b], P.J. Morrison[b], H.-B. Park[a], and D.-I. Choi[a]

a Department of Physics, Korea Advanced Institute of Science and Technology, Taejon 305-701, Korea

b Institute for Fusion Studies, University of Texas at Austin, Austin, Texas 78712, U.S.A.

Abstract

Global drift wave map equations that allow the integration of particle orbits on long time scales are implemented to describe transport. Ensembles of test particles are tracked to simulate the Low-confinement mode/Reversed Shear/Enhanced Reversed Shear plasmas in Tokamak Fusion Test Reactor(TFTR) tokamak and the Optimized Shear plasma in Joint European Torus(JET) tokamak. The simulations incorporate a radial electric field, $\overline{E}_r$, obtained from a neoclassical calculation [Zhu *et al.*, Phys. Plasmas **6**, 2503 (1999)] and a model for drift wave fluctuations that takes into account change in the mode structure due to $\overline{E}_r$ [Taylor *et al.*, Plasma Phys. Controlled Fusion **38**, 1999 (1996)]. Steady state particle density profiles along with two different measures of transport, the diffusion coefficient based on a running time average of the particle displacement and that calculated from the mean exit time, are obtained. For either weak or reversed magnetic shear and highly sheared $\overline{E}_r$, particle transport barriers are observed to be established. In the presence of such a transport barrier, it is shown that there is, in general, a difference between the two measures of transport. The difference is explained

by a simple model of the transport barrier.

52.80.Pi, 52.50.-b, 52.65.+z, 52.75.-d

I. INTRODUCTION

Recently, there have been experimental reports of strongly improved particle confinement in tokamak plasmas [1–3]. These reports indicate that particle transport behaves as if a barrier exists in very weak or zero magnetic shear regions, resulting in a transport level that is reduced to nearly the neoclassical prediction, or even lower, in the core region of the tokamak. Also, the formation of strong equilibrium radial electric fields, $\overline{E}_r$, are observed. From these observations it is thought that the great improvement in particle confinement results from the suppression of drift wave turbulence, which is now well established as the principal mechanism for causing anomalous transport in tokamak plasmas [4].

In Ref. [5], it was shown that very weak or zero magnetic shear can reduce the particle transport substantially without a significant change in the turbulence level, using newly derived drift wave maps. These drift wave maps are area preserving maps for the guiding center motion of particles in drift wave turbulence. Specific drift wave maps were shown to have the form of the standard nontwist map for the reversed shear(RS)/ enchanced reversed shear(ERS) plasmas [6–8]. Such nontwist maps possess winding number profiles that are nonmonotonic, and sturdy invariant tori associated with extrema of such profiles provide transport barriers. Also in Ref. [5], it was shown that highly sheared radial electric fields, ones with $|v_\parallel| \sim c|\overline{E}_r/B_\vartheta|$, where $|v_\parallel|$ is the parallel ion thermal velocity and B_ϑ is poloidal magnetic field, can reduce the transport level by phase decorrelation between particle guiding centers and drift wave fluctuations. The demonstration of reduced transport was possible because the drift wave maps allow very long time integration of particle orbits in comparison to solving the exact guiding center orbit equations. However, it was not possible in Ref. [5] to locate the transport barrier in detail because of the lack of a reliable global model for the drift wave mode structure and because of the absence of a good $\overline{E}_r$ model.

In the present work, we perform new test particle transport simulations that show clearly the formation of the transport barrier. We investigate the location of the particle transport barrier with the influence of $\overline{E}_r$ on the drift wave mode structure. For this purpose a global

model for the drift wave mode structure and a neoclassical model for the radial electric field $\overline{E}_r$ are taken from well developed theories. For the global drift wave structure we adopt the analytical model of Ref. [9], while for $\overline{E}_r$ we use the results from the neoclassical calculation of Ref. [10].

A test particle simulation using the exact guiding center orbit equations for finding the location of transport barrier is computationally unfeasable because local transport properties are needed. Generally, the calculation of such transport properties from test particle simulations relies on the ergodicity property of an ensemble of particles evenly distributed over the whole region of phase space, which inevitably leads to globally averaged quantities. However, if we can calculate the particle density profile directly, this difficulty does not occur. The drift wave maps make it possible to integrate a very large number of particles for the long transport time scale under fairly complicated forms of the drift wave mode structure. Thus, the drift wave map allows us to calculate the steady state particle density profiles directly.

Although it is generally hard to infer local transport information from globally averaged quantities, we will show that in some special cases it is possible in an indirect way to obtain this information by comparing two different measures of a global transport quantity. Namely, we calculate the diffusion coefficient based on a running time average of the square of the particle displacement and a second diffusion coefficient calculated from the mean exit time. In general these two quantities differ. We present a theory that explains the relationship between these two measures of transport and the formation of a transport barrier.

This paper is organized as follows. In Sec. II the drift wave map equations and assumptions for their derivations are briefly reviewed. In Sec. III the drift wave model that is used in the simulations is described. In Sec. IV the procedures for the test particle simulations are described, including a Monte Carlo map for pitch angle scattering that is used in conjunction with a drift wave map. Here the particle diffusion coefficients and the steady state particle density profiles are obtained. In Sec.V we present a simple theory to explain the results in Sec. IV. Finally, we summarize and conclude in Sec. VI.

II. DRIFT WAVE MAP

The justification for extracting maps, such as the standard map, from differential equations that describe particle dynamics is based on the assumption that the force is composed of waves with a broadband spectrum. Such forces phase mix to zero except for temporally localized impulsive jumps, between which the differential equations can be easily integrated to yield the map. The physical motivation and justification given in Ref. [5] for introducing drift wave maps in place of the differential equations was based on electromagnetic (laser and microwave) scattering experiments, which show a wide frequency spectrum for a fixed scattering wave vector $\boldsymbol{k}$ [11,12]. Indeed many experiments show a broad drift wave frequency spectrum with substantial amplitudes for frequencies $n\omega$ with $n = 1, 2, \ldots K$ for K large.

Two kinds of drift wave maps were introduced in Ref. [5], local and global. Local drift wave map equations were derived by idealizing the finite mode drift wave spectrum,

$$\widetilde{\phi}(\boldsymbol{x}, t) = \sum_{n=-K}^{K} \phi_{M,L} \cos(M\vartheta - L\varphi - n\omega t), \tag{1}$$

by taking the limit $K \to \infty$. In this way one obtains the impulsive jumps that lead to the mapping equations,

$$I_{N+1} = I_N + \frac{4\pi c}{a^2 B_0} \frac{M\phi_{M,L}}{\omega} \sin(\psi_N), \tag{2}$$

$$\psi_{N+1} = \psi_N + R_1(I_{N+1}) + R_2(I_{N+1}), \tag{3}$$

$$R_1(I) = \frac{v_\parallel(I)}{\omega q(I) R_0} \left[M - Lq(I)\right], \tag{4}$$

$$R_2(I) = -\frac{cM}{\omega a B_0} \frac{\overline{E}_r(I)}{\sqrt{I}}, \tag{5}$$

$$v_\parallel(I) = \sqrt{\frac{2}{m} \left[\mathcal{E} - e\Phi_0(I)\right] \left[1 - \lambda B_0\right]}, \tag{6}$$

for advancing the guiding centers over successive correlation times $2\pi/\omega$. Here, a and R_0 are the minor and major radii, respectively, q is the safety factor, $I = (r/a)^2$, $\psi = M\vartheta - L\varphi$, B_0 is the magnitude of the magnetic field at the magnetic axis, m and e are the mass and the

charge of the particle, respectively, $\mathcal{E}$ is the total energy, the equilibrium radial electric field is related to the electrostatic potential according to $\overline{E}_r(I) = -\partial\Phi_0/\partial r|_{r=a\sqrt{I}}$, and $\lambda = \mu/\mathcal{E}_k$, where $\mathcal{E}_k$ is the kinetic energy of the particle and μ is the magnetic moment. The poloidal and toroidal mode numbers of the localized drift wave fluctuation are denoted by M and L, respectively. The map equations (2) and (3) are area preserving and the Hamiltonian map structure of these equations was investigated for various forms for the radial electric field and q-profile.

For a reversed shear magnetic field configuration, this local map reduces to the standard nontwist map (SNM) when expanded around $r_{\min}$, where $q'(r_{\min}) = 0$. For the SNM, the relative rareness of low order resonant rational surfaces and the small size of high order resonances cause a robustness of the tori near $r_{\min}$. The presence of these robust or sturdy tori was shown to produce a strongly reduced transport rate, without a significant change in the drift wave fluctuation level at each mode rational surface. This suppression of the transport level by weak shear was suggested as the reason for the formation of the transport barrier in the ERS experiment [5].

Although the local map equations are useful for studying local transport, after many iterations particles eventually leave a neighborhood of the drift wave, and thus one must extend the drift wave model to include global radial variation. An appropriate global model is that of Connor and Taylor [13] for drift wave fluctuations of frequency ω and an infinite frequency spectrum $n\omega$, $n = \pm 1, \pm 2, ...$,

$$\begin{aligned}\widetilde{\phi} = \widetilde{\phi}_0 \sum_{n=-\infty}^{\infty} \sum_{L} \sum_{m=m_1}^{m_2} & \exp[\sigma_I (x-m)^2/2] \\ & \times \cos[-\sigma_R (x-m)^2/2 - (m+M)\vartheta + L\varphi - n\omega t]\,. \end{aligned} \tag{7}$$

Here $\widetilde{\phi}_0$ is the mode amplitude, $\sigma = \sigma_R + \sigma_I$ depends upon the diamagnetic frequency, the density scale length, and other plasma parameters (see Refs. [5] or [13] and Sec. III), $x = k\rho s$, where $\rho = r_0 - r$ with r_0 defined by $M/L = q(r_0)$, $k = Lq/r$, and $s(r) = (r/q)(dq/dr)$. In Ref. [5] (7) was used to obtain the global map equations given by

$$I_{N+1} = I_N + \frac{4\pi c}{\omega a^2 B_0} \frac{\partial \widetilde{\phi}}{\partial \vartheta}(I_{N+1}, \vartheta_N, \varphi_N)\,, \tag{8}$$

$$\vartheta_{N+1} = \vartheta_N + \frac{2\pi}{R_0 \omega}\left[\frac{v_\parallel}{q(I_{N+1})} + \frac{2cR_0}{B_0 a^2}\left(\frac{\partial \widetilde{\phi}}{\partial I}(I_{N+1}, \vartheta_N, \varphi_N) - \overline{E}_r(I_{N+1})\right)\right]\,, \tag{9}$$

$$\varphi_{N+1} = \varphi_N + \frac{2\pi v_\parallel}{R_0 \omega}\,. \tag{10}$$

The map defined by Eqs. (8)–(10) can be viewed as a four-dimensional symplectic map associated with a two degree-of-freedom Hamiltonian system, where the fourth map variable, the momentum conjugate to φ, is ignorable. Alternatively, Eqs. (8)–(10) can be viewed as a time dependent two-dimensional symplectic or area preserving map. This is seen by solving (10), which gives $\varphi_N = 2\pi N v_\parallel/(R_0\omega)$ when $v_\parallel$ is constant, and inserting this result into Eqs. (8) and (9). The resulting two equations are area preserving because they can be derived from a mixed variable generating function according to $I_N = \partial\mathcal{F}/\partial\vartheta_N$ and $\vartheta_{N+1} = \partial\mathcal{F}/\partial I_{N+1}$, where $\mathcal{F} = \mathcal{F}(I_{N+1}, \vartheta_N, N)$. We leave the map in the form of Eqs. (8)–(10) because in Sec. IV we allow $v_\parallel$ to change by collisions.

In order to identify the location of the particle transport barrier an even more reliable global drift wave model, one that takes into account the density of rational surfaces and the modification of the mode structure due to $\overline{E}_r$, is needed. In the next section, we describe the global model of drift wave fluctuations that is used here in our test particle simulations.

III. DRIFT WAVE MODEL

Early work on drift wave fluctuations dealt with radially localized modes that arise at special radial points of the equilibrium profiles; for example, in the case of electron-drift modes these special points occur at the position of the maximum diamagnetic frequency ω_{*e} [14,15]. Recently, another drift wave branch, composed of the so-called generalized modes, has been discovered and, in contrast to the localized modes, proposed as the principal cause of anomalous transport [16]– [18]. These new modes have a higher magnetic shear damping rate than the localized modes and can arise at any rational surface. As explained in our study of the local map, the relative rareness of resonant rational surfaces, i.e. the low

density of rational surfaces in the weak shear region, is believed to be one of the reasons for transport reduction by weak shear [19], which also underscores the importance of the generalized modes since they can arise at arbitrary rational surfaces. In this work, we study the particle transport produced by these generalized modes.

For determination of the drift wave mode structure, another important element that must be considered is the $\overline{E}_r$-generated poloidal flow. As mentioned in Sec. I, in ERS and other high confinement experiments, there are indications that large equilibrium radial electric fields exist. There have been many studies of the role of $\overline{E}_r$ on the drift wave mode structure [9,20], and these studies show that the dependence of the mode width on the ion Larmor radius is reduced from $\rho_i^{1/2}$ to ρ_i, which also implies a reduction of the transport level. Recently, the radial electric field for reversed magnetic shear discharges has been calculated using neoclassical theory with the impurity rotational velocity [10]. These calculations show that a reduced analytic formula for $\overline{E}_r$ obtained in Ref. [21] over estimates its magnitude and gradient. For this reason, we use the result of Ref. [10] and the same Tokamak Fusion Test Reactor(TFTR) database for the present problem.

To determine the parameters for the mode structure of the drift wave fluctuations, we proceed in the same way as that of Ref. [9]. We start from the model equation for short-wavelength plasma fluctuations with large toroidal eigenmode number $L \gg 1$ in a large aspect ratio torus:

$$\left[\frac{1}{(Lq')^2}\frac{\partial^2}{\partial\rho^2} - \sigma^2\left(\frac{\partial}{\partial\vartheta} + iLq'\rho\right)^2 - \alpha\left(\cos\vartheta + \frac{is}{Lq'}\sin\vartheta\frac{\partial}{\partial\rho}\right) - \Lambda\right]\widetilde{\phi}(\rho,\vartheta) = 0, \tag{11}$$

where

$$s = \frac{rq'}{q}, \quad \sigma = \frac{L_n}{bqsR\Omega}, \quad \alpha = \frac{2L_n}{bs^2R\Omega}, \quad \tau = \frac{T_e}{T_i}, \tag{12}$$

$$b = \frac{1}{2}k_\vartheta^2\rho_i^2, \quad k_\vartheta = \frac{M}{r_0}, \quad \Omega = \frac{\omega}{\omega_{*e}}, \quad \eta_i = \frac{L_n}{L_T}, \tag{13}$$

$$\Lambda = \frac{1}{bs^2}\left[\frac{\tau(\Omega-1)}{\tau+\eta_i+1} + b\right]. \tag{14}$$

As in Sec. II, $\rho = r - r_0$ is the distance from the rational surface where the mode is centered where $q(r_0) = M/L$. The quantity α measures the strength of the toroidicity induced mode

coupling. Inclusion of poloidal plasma rotation, v_E, due to the radial electric field introduces a Doppler shift in ω,

$$\omega - \boldsymbol{k}\cdot\boldsymbol{v}_E = \omega - k_\vartheta v_E \approx \omega - k_\vartheta(v_{E0} + v'_E\rho)\,, \tag{15}$$

where $v_E(r)$ is expanded around $\rho = 0$. Also, we assume a linear variation of $\omega_{*e}(r)$ for the modeling of the generalized mode,

$$\omega_{*e} \approx \omega_{*e0} + \frac{d\omega_{*e}}{dr}\Big|_{r=r_0}\rho = \omega_{*e0}\left(1 + \frac{\rho}{L_*}\right), \tag{16}$$

where $1/L_* \equiv \omega_{*e0}^{-1}\, d\omega_{*e}/dr\Big|_{r=r_0}$. With this assumption Eq. (11) becomes

$$\left[\frac{\partial^2}{\partial x^2} - \sigma^2\left(\frac{\partial}{\partial\vartheta} + ix\right)^2 - \alpha\left(\cos\vartheta + is\sin\vartheta\frac{\partial}{\partial x}\right) - \Lambda + \kappa x\right]\widetilde{\phi}(x,\vartheta) = 0\,, \tag{17}$$

where $x = Lq'\rho$, $\kappa = \kappa_1 + \kappa_2$, and

$$\kappa_1 = \frac{\tau\Omega_s}{Lq'bs^2L_*(\tau + \eta_i + 1)}, \quad \kappa_2 = \frac{\tau}{Lq'bs^2L_E(\tau + \eta_i + 1)}. \tag{18}$$

In Eq. (18) we define $1/L_E \equiv k_\vartheta v'_{E0}/\omega_{*e0}$ and $\Omega_s \equiv (\omega - k_\vartheta v_{E0})/\omega_{*e0} \approx 1$. The quantity κ_1 measures the shearing due to the gradient of ω_{*e}, while κ_2 measures the shearing due to the $\boldsymbol{E}\times\boldsymbol{B}$ Doppler shift.

Upon Fourier expanding the potential $\widetilde{\phi}$ in the poloidal angle ϑ,

$$\widetilde{\phi}(x,\vartheta) = \sum_m c_m\phi_m(x)e^{-im\vartheta}, \tag{19}$$

and projecting Eq. (17) onto the m-th harmonic, we obtain

$$c_m(L_m - \Lambda)\phi_m - \frac{\alpha}{2}\sum_{\pm}\left[c_{m\pm1}\left(\phi_{m\pm1} \mp s\frac{\partial\phi_{m\pm1}}{\partial x}\right)\right] = 0\,, \tag{20}$$

where the operator L_m is defined by

$$L_m \equiv \left[\frac{\partial^2}{\partial x^2} + \sigma^2(x-m)^2 + \kappa x\right]. \tag{21}$$

As in Ref. [9], we assume $\alpha \sim \kappa \ll 1$ and write $\phi_m = \phi_m^0 + \phi_m^1$, where an ordering in α is assumed. Writing $L_m = L_m^0 + L^1$, where $L_m^0 \equiv \partial_x^2 + \sigma^2(x-m)^2$ and $L^1 \equiv \kappa x$, we obtain the following zeroth order solution of Eq. (20):

$$\phi_m^0(x) = \exp\left[-i\frac{\sigma}{2}(x-m)^2\right], \tag{22}$$

$$\lambda_0 = -i\sigma \approx \frac{1}{bs^2}\left[\frac{\tau(\Omega_s - 1)}{\tau + \eta_i + 1} + b - i\delta\right], \tag{23}$$

where $L_m^0\phi_m^0 = \lambda_0\phi_m^0$. Here $i\delta$ is included so that σ^2 has a small negative imaginary part [4], which physically represents the destabilizing effect of electron Landau resonance or trapped electrons [13].

To zeroth order, all the modes of Eqs. (22)-(23) are degenerate, and we must proceed to first order to remove the degeneracy and obtain the relationship between c_m's. The first order equation is

$$c_m(L_m^0 - \Lambda)\phi_m^1 + c_m(\lambda_0 + L^1 - \Lambda)\phi_m^0 - \frac{\alpha}{2}\sum_{\pm}\left[c_{m\pm1}\left(\phi_{m\pm1}^0 \mp s\frac{\partial\phi_{m\pm1}^0}{\partial x}\right)\right] = 0\,. \tag{24}$$

The solvability condition for (24) is obtained by multiplying by ϕ_m^0 and integrating over x, which gives

$$(\lambda_0 + m\kappa - \Lambda)c_m = \frac{\alpha V}{2}(c_{m+1} + c_{m-1}), \tag{25}$$

where

$$V \equiv \left[\int \phi_m^0\left(\phi_{m+1}^0 - s\frac{\partial\phi_{m+1}^0}{\partial x}\right)dx\right]\left[\int(\phi_m^0)^2 dx\right]^{-1}. \tag{26}$$

The solution to Eq. (25) can be obtained easily by using the generating function $g(u) = \sum_m c_m \exp(-imu)$. Upon multiplying (25) by $\exp(-imu)$, summing over m, and manipulating, the equation for $g(u)$ is seen to be

$$i\kappa\frac{d}{du}g(u) + [\lambda_0 - \Lambda - \alpha V\cos(u)]\,g(u) = 0, \tag{27}$$

which has the solution

$$g(u) = \exp\left(i\left[\frac{(\lambda_0 - \Lambda)u}{\kappa} - \frac{\alpha V}{\kappa}\sin u\right]\right). \tag{28}$$

This expression for $g(u)$ can be easily inverted to obtain c_m by using the generating function for the Bessel function J_m. This gives

$$c_m = J_m(\alpha V/\kappa)\,, \tag{29}$$

using $\lambda_0 = \Lambda$, which is valid to lowest order.

If κ is large, only a few neighboring modes will be excited. For weak shear in v_E' and ω_{*e}, the parameter κ is small, and the number of modes that are significantly coupled to mode-m becomes large. Asymptotically, the number of coupled modes is given by

$$\Delta m \sim |\alpha V/\kappa|^{1/2}. \tag{30}$$

Summarizing, the model drift wave spectrum is given by

$$\begin{aligned}\widetilde{\phi} = \widetilde{\phi_0} \sum_{n=-\infty}^{\infty} \sum_{L} \sum_{m=m_1}^{m_2} \exp\left[\frac{\sigma_I}{2}(x-m)^2\right] \\ \times \cos\left[-\frac{\sigma_R}{2}(x-m)^2 - (m+M)\vartheta + L\varphi - n\omega t\right],\end{aligned} \tag{31}$$

where $\widetilde{\phi}_0$ is the mode amplitude, σ is determined by Eq. (23), and $|m_1| \sim |m_2| \sim |\alpha V/\kappa|^{1/2}$. Here, the limit of an infinite frequency spectrum $n\omega$, $n = \pm 1, \pm 2, ...$ is assumed for the derivation of map equations and multiple toroidal mode numbers (sum over L) are also included. This form represents a ballooning mode centered at $r = r_0$ with $m_2 - m_1 + 1$ sidebands. The radial width is approximately given by the distance between the two outer most rational surfaces for the sidebands with mode numbers $(M+m_1, N)$ and $(M+m_2, N)$.

The drift wave amplitude $\widetilde{\phi}_0$ is determined by

$$\widetilde{\phi}_0 = C\frac{l_c}{L_{T_i}} T_e\,, \tag{32}$$

where l_c is the mixing length and L_{T_i} is the ion temperature gradient length scale. Here we use the Ottaviani-Horton-Erba (OHE) model, which gives $l_c = q\rho_s R/L_{T_i}$ [22]. Each ballooning mode has $m_2 - m_1 + 1$ sidebands, and therefore an effective fluctuation amplitude for the ballooning mode is approximately given by $N_T \times (m_2 - m_1 + 1) \times \widetilde{\phi}_0$, where N_T is the number of different toroidal modes. The constant factor C is introduced to place this value in the appropriate range, and is chosen to be $C \sim 1/\left(N_T \times (m_2 - m_1)\right)$.

Within the ordering used for the derivation of the drift wave model, $b \sim L_n/R \sim \delta \ll 1$ and σ is given approximately by

$$\sigma \approx \frac{L_n}{bqsR}\left[1 + i\left(\delta - \frac{\tau + \eta_i + 1}{\tau}\frac{sL_n}{qR}\right)\right]^{-1} \approx \frac{L_n}{bqsR}\left[1 - i\left(\delta - \frac{L_n s}{qR}\right)\right]. \tag{33}$$

If we consider only the shear damping term, $L_n s/qR$, then the absolute value of the imaginary part of σ becomes

$$|\sigma_I| \approx \frac{L_n^2}{bq^2R^2} = \frac{2L_n^2}{q^2R^2k_\vartheta^2\rho_i^2}\,, \tag{34}$$

by the definition of σ and Eq. (23). Since the radial variation of a single sideband is approximately $\exp\left[-|\sigma_I|k_\vartheta^2 s^2(r-r_m)^2/2\right]$, where $q(r_m) = (M+m)/L$, its radial width is given by

$$\Delta r_w = \sqrt{\frac{2}{|\sigma_I|k_\vartheta^2 s^2}} = \frac{qR\rho_i}{L_n|s|}\,. \tag{35}$$

Note that this expression fails as one approaches $r_{\min}$, since $s \to 0$. This divergence is caused by the fact that s in all of the above formulas is set to a constant value at the rational surface through r_0 where the modes are centered. To remove this divergence, one must allow a radial variation of s, but a detailed consideration is beyond the scope of the present work. Here we give an estimate of the minimum allowable distance between $r_{\min}$ and the nearest sideband within which our model is plausible. Upon expanding s around $r_{\min}$, using $s = s'_{\min}\Delta r$, and setting $\Delta r_w = \Delta r$, we obtain

$$(\Delta r)_{\min} \approx \sqrt{\frac{\rho_i qR}{L_n|s'_{\min}|}}. \tag{36}$$

The estimate of (36) is used for determining the drift wave mode structure near $r_{\min}$.

For global modeling of the drift wave, particularly for the generalized mode, one must, in principle, assign modes to all of the rational surfaces. However, this procedure is impossible in practice, so here we choose rational surfaces in a manner based on the density of rational surfaces of the given q-profile. In particular, modes are placed on rational surfaces so that q-values are nearly equally spaced.

We carry out our simulations for three different cases that correspond to TFTR and Joint European Torus(JET) discharges. We use $R_0 = 260\,\mathrm{cm}$, $a = 94\,\mathrm{cm}$, and $B_0 = 4.6\,\mathrm{T}$ for

TFTR, and $R_0 = 307.6\,\mathrm{cm}$, $a = 94\,\mathrm{cm}$, and $B_0 = 3.57\,\mathrm{T}$ for JET. According to the ordering in the drift wave model, b and Ω satisfy $b = k_\vartheta^2 \rho_i^2/2 \sim \epsilon \ll 1$ and $\Omega = \omega/\omega_{*e} \sim 1$. We can determine the parameters L and ω using these relations. Although, these parameters are different for the following three cases, their order of magnitude are similar and approximately given by $L \sim 40$ and $\omega \sim 2.5 \times 10^4\,\mathrm{sec}-1$ for Case I and $L \sim 20$ and $\omega \sim 5 \times 10^4\,\mathrm{sec}^{-1}$ for Case II and Case III. In the following simulations, multiple toroidal mode numbers of $L = 40, 43, 46$ are chosen for Case I and $L = 20, 22, 25$ for Case II and Case III. ω is set to $2.5 \times 10^4\,\mathrm{sec}^{-1}$ for Case I and $5.0 \times 10^4\,\mathrm{sec}^{-1}$ for Case II and Case III.

- Case I

  This is the case of an Low-confinement mode (L-mode) plasma on TFTR (shot number #50911), which has a monotonically increasing q-profile and dose not have an appreciable $\overline{E}_r$. The data is taken from U-files in Iternational Thermonuclear Experimental Reactor(ITER) database.

- Case II

  This is the case of an ERS plasma on TFTR (shot number #88299). This plasma has a reversed shear q-profile and large $\overline{E}_r$. The $q_{\min}$ is located at $r = 0.35a$ and the region where $\overline{E}_r$ is highly sheared is mostly inside $r = 0.4a$. This data is obtained from Budny in PPPL.

- Case III

  This is the case of optimized shear plasma experiment on JET (shot number #40542) [3]. In this case, the q-profile is not reversely sheared. But it is nearly flat in $r < 0.45a$. Also the plasma has large positive $\overline{E}_r$ which is highly sheared in $r < 0.6a$. All neutral beams are coinjected parallel to the plasma current. This data is also taken from U-files in ITER database.

In Fig. 1, plasma profiles are plotted for each case. In the figure, triangular and circular dots represent experimental data and solid curves are fitted profiles used in the simulations.

These profiles determine the drift wave parameters. Square points on the q-curves represent the selected rational surfaces on which drift wave modes are assigned. Figure 2 contains plots of $\overline{E}_r$ for Case II and Case III. Figures 3-5 show plots of the parameter $|\alpha V/\kappa|$ for the three cases. From the figures it can be seen that the decrease of the mode widths caused by $\overline{E}_r$ is appreciable for $r < 0.35a$ in Case II, and for $r < 0.55a$ in Case III.

IV. TEST PARTICLE SIMULATION

In our test particle simulations, a Monte Carlo Coulomb collisional pitch angle scattering map is used in conjunction with the map equations of Sec. II. Assuming that small angle Coulomb scattering changes the direction, but not the magnitude, of the velocity, the collisional scattering map for the change of velocity was derived in Ref. [23] and is given by the following:

$$(\rho_\parallel)_f = (\rho_\parallel)_i \cos\gamma_1 + \sqrt{\frac{2\mu_i}{B_i}} \sin\gamma_1 \cos\gamma_2, \tag{37}$$

$$\begin{aligned} \frac{2\mu_f}{B_f} &= \left((\rho_\parallel)_i^2 + \frac{2\mu_i}{B_i} \right) \sin^2\gamma_1 \sin^2\gamma_2 \\ &\quad + \left(\sqrt{\frac{2\mu_i}{B_i}} \cos\gamma_1 - (\rho_\parallel)_i \sin\gamma_1 \cos\gamma_2 \right)^2, \end{aligned} \tag{38}$$

where the subscripts i and f refer to values before and after the collision, respectively. Here $\rho_\parallel \equiv v_\parallel/\Omega_i$, Ω_i is the ion gyrofrequency on the magnetic axis, and $\mu \equiv mv_\perp^2/2B$ is the magnetic moment. The two angles γ_1 and γ_2 are determined from

$$\gamma_1 = [-\nu\delta t \ln(1-\eta_1)]^{1/2}, \qquad \gamma_2 = 2\pi\eta_2, \tag{39}$$

where η_1 and η_2 are two random numbers that are assumed to be uniformly distributed on $[0,1]$. Here ν is the collision rate, δt is the simulation time step, and $\nu\delta t \ll 1$ is required. Because of the randomness associated with the parameters η_1 and η_2, the collision map is an example of a dynamical system with extrinsic chaos or stochasticity.

The particle simulation is carried out as follows. For each time step, the collision map is applied to the velocity of each particle. Then, the changed velocity is used in the next iteration of the drift wave map equations of (8)–(10). The process is repeated. Initially, we locate 32768 D^+ ions at $r = 0.05a$, and the initial pitch parameter is set to $\lambda = 0.0$. The initial kinetic energy is set to 4.5 keV for Case I and 22 keV for Case II and Case III according to the core ion temperatures of the experimental data. However, this choice of initial kinetic energy does not much affect the final results in these map simulations, because local diffusion coefficient is independent of $v_{\|}$ after onset of diffusion(see Ref. [5]) and the extrinsic stochasticity by the collision map satisfies the condition for onset of diffusion. Particle positions are advanced in time using the alternation of the drift wave and collision maps until they reach the limiter at $r = 0.95a$. Once a particle reaches the limiter, it is treated as lost and a new particle is born again at the core in the same way. This procedure is continued in anticipation of a steady state. To determine whether our particle ensemble has reached a steady state, we check to see if the particle fluxes at two positions, $r = 0.4a$ and $r = 0.95a$, are the same. In Figs. 6, 8, and 10, particle fluxes at these positions are plotted for our three cases. Evidently, the fluxes have saturated, since the fluxes measured at the two different positions are nearly same.

The two diffusion coefficients are calculated as follows. First, we calculate the usual diffusion coefficient using

$$D(t) = \frac{1}{2t}\frac{1}{N}\sum_{j=1}^{N}[r_j(t) - r_j(0)]^2 \tag{40}$$

for the ensemble of D^+ ions. In Figs. 7(a), 9(a), and 11(a) the time series of $D(t)$ is plotted for the three cases. The quantity $D(t)$ converges to a well-defined constant values, indicating that the radial transport is indeed a diffusion process. Specifically, we obtain the diffusion coefficient from the time series of $D(t)$ by using

$$\overline{D} = \frac{1}{T - T_0}\int_{T_0}^{T} D(t)dt\,, \tag{41}$$

where T_0 is the time at which convergence is observed to set in.

To obtain the second diffusion coefficient, we calculate the average confinement (mean exit) time $\langle\tau_{\rm ext}\rangle$ and then use it to obtain a diffusion coefficient defined by $D_{\rm ext} = a^2/2\langle\tau_{\rm ext}\rangle$. In Figs. 7(b), 9(b), and 11(b), $\langle\tau_{\rm ext}\rangle$ is plotted versus time. For $D_{\rm ext}$ calculations, we use the values of $\langle\tau_{\rm ext}\rangle$ at the final time.

Table 1 shows $\overline{D}$ and $D_{\rm ext}$ for our three cases. The values in parentheses are cases where $\overline{E}_r$ is included. We see that both $\overline{D}$ and $D_{\rm ext}$ for Case II and Case III are smaller than those for Case I. Also, for Case II and Case III, we see that the transport is reduced by the inclusion of $\overline{E}_r$. Note that the difference between $\overline{D}$ and $D_{\rm ext}$ varies for each case, but $D_{\rm ext} > \overline{D}$ for all cases. The difference is small in Case I and becomes larger in the other two cases where there is important confinement. We will show that the difference is related to the formation of internal transport barriers. A detailed explanation will be given in the next section.

Finally, we calculate steady state particle density profiles in the following way. The minor radius is divided into 120 radial bins with equal radial widths, and the number of particles in each radial bin is counted after the particle flux has reached the saturated value. The bin numbers obtained in this way are then divided by the volume of the corresponding radial bin and finally normalized so that the total number of particles is unity. In Fig. 12, the particle density profiles are plotted for the three cases. We see that the density in Fig. 12(b) and Fig. 12(c) drops abruptly compared to that of Fig. 12(a), which indicates the existence of transport barriers in the former two cases. The former two cases have zero or very weak magnetic shear regions and the points where the density profiles drop coincide with the boundaries of these regions. If we include $\overline{E}_r$, the transport barrier for the JET case moves outward and particle confinement is further improved. But, the transport barrier for TFTR is mostly unchanged. This is because the region where $\overline{E}_r$ is highly sheared is nearly the same as the region where the magnetic shear reverses. However, as we have mentioned above, particle transport is reduced.

V. TRANSPORT BARRIER AND INHOMOGENEITY IN THE LOCAL DIFFUSION COEFFICIENT

In general, the anomalous diffusion caused by electrostatic drift waves is highly inhomogeneous because of the radial variation of the drift wave fluctuation amplitude and correlation length. However, if there exists a transport barrier, small inhomogeneities of the ambient fluctuations may not be noticeable, and only a big difference between the local transport properties inside and outside of the transport barrier will matter. Here, we model such a situation using a one-dimensional diffusion equation with a spatially varying diffusion coefficient:

$$\frac{\partial n}{\partial t} = \frac{\partial^2}{\partial r^2}\left[D(r)n\right] \ , \tag{42}$$

where

$$D(r) = \begin{cases} D_1 & \text{if } |r| < r_b \\ D_2 & \text{if } r_b \leq |r| < a \, . \end{cases} \tag{43}$$

Equation (43) is a Fokker–Planck equation in the absence of drag, which is further discussed in the Appendix. In Sec. IV, $\overline{D}$ was calculated by using a constant source at the center and a sink at the edge. This situation can be represented by including a δ-function source term located at the core and by imposing a vanishing boundary condition at $r = \pm a$,

$$\frac{\partial n}{\partial t} = \frac{\partial^2}{\partial r^2}\left[D(r)n\right] + p\delta(r) \, . \tag{44}$$

Here p is the particle production rate at the core. With the boundary condition $n(\pm a) = 0$, a steady state solution can be obtained readily,

$$n(r) = \begin{cases} -\frac{p}{2D_1}|r| + \left(\frac{p}{2D_1} - \frac{p}{2D_2}\right) r_b + \frac{pa}{2D_2} & \text{if } |r| < r_b \\ -\frac{p}{2D_2}|r| + \frac{pa}{2D_2} & \text{if } r_b \leq |r| < a \, . \end{cases} \tag{45}$$

The total number of particles $\mathcal{N}$ is given by

$$\mathcal{N} = \int_{-a}^{a} n(r)dr = \frac{p\left[D_1 a^2 + (D_2 - D_1) r_b^2\right]}{2D_1 D_2}, \tag{46}$$

and the ensemble average of the local diffusion coefficient $D(r)$ is given by

$$\overline{D} = \frac{1}{\mathcal{N}} \int_{-a}^{a} D(r) n(r) dr = \frac{D_1 \left[D_2 a^2 + 2(D_1 - D_2) a r_b + 2(D_2 - D_1) r_b^2 \right]}{D_1 a^2 + (D_2 - D_1) r_b^2}. \tag{47}$$

It is clear that in the steady state, this ensemble average must give the same result for $\overline{D}$ as that obtained from Eq. (41).

Our next job is the calculation of τ_{ext} and, hence, D_{ext}. The mean exit time of the particles undergoing random motion is given by the solution of Dynkin's equation, which involves the adjoint of the operator of Eq. (42). In the Appendix, the theory is explained in greater detail. For our problem, Dynkin's equation takes a very simple form,

$$D(r) \frac{\partial^2 u}{\partial r^2} = -1, \qquad |r| < a \tag{48}$$

where u, a variable that can be related to the mean exit time, satisfies the boundary condition $u(\pm a) = 0$. The solution of Eq. (48) is given by

$$u(r) = \begin{cases} -\frac{r^2}{2D_1} + \frac{(a^2 - r_b^2)}{2D_2} + \frac{r_b^2}{2D_1} & \text{if } |r| < r_b \\ \frac{(a^2 - r^2)}{2D_2} & \text{if } r_b \leq |r| < a \end{cases} \tag{49}$$

and we have

$$\langle \tau_{\text{ext}} \rangle = u(0) = \frac{(a^2 - r_b^2)}{2D_2} + \frac{r_b^2}{2D_1}, \tag{50}$$

and

$$D_{\text{ext}} = \frac{a^2}{2\langle \tau_{\text{ext}} \rangle} = \frac{D_1 D_2 a^2}{D_1 a^2 + (D_2 - D_1) r_b^2}. \tag{51}$$

The difference between D_{ext} and $\overline{D}$ is given by

$$D_{\text{ext}} - \bar{D} = 2D_1 \frac{(d-1)(x_b - x_b^2)}{1 + (d-1) x_b^2}, \tag{52}$$

where $d \equiv D_2/D_1$ and $x_b \equiv r_b/a < 1$. Note that this expression is always positive if $D_2 > D_1$. Generally, the local diffusion coefficient increases as one approaches the tokamak edge [24]. In particular, if there exists a transport barrier, this is the case that we actually meet. Note also that if $D_2 = D_1$, i.e. the diffusion is nearly homogeneous, then the difference

vanishes. In Sec.IV, the difference between $D_{\rm ext}$ and $\overline{D}$ for Case I is the smallest, so we can interpret this as an indication of a more homogeneous radial diffusion as compared to the other two cases.

VI. CONCLUSION

We have carried out global test particle simulations for three tokamak confinement regimes. The simulations incorporate drift wave fluctuations derived from a linear superposition of the generalized toroidal mode [18], with the modification due to $\overline{E}_r$ [9] taken into account. Using $\overline{E}_r$ obtained from neoclassical theory with the measured impurity rotational velocity [10], rotational invariance was removed, and we have demonstrated the suppression of drift wave transport for weak and reversed magnetic shear.

To study the formation and location of particle transport barriers, knowledge of local particle transport is required, and we chose to calculate the particle density profile directly. A direct density profile calculation was facilitated by employing drift wave and collision maps [5]. Two diffusion coefficients were calculated. One based on the running time average of the particle displacement, $\bar{D}$, and the other based on the mean exit time, $D_{\rm ext} = a^2/2\langle\tau_{\rm ext}\rangle$. The simulations demonstrated that reversed or very weak magnetic shear can reduce the particle transport by establishing a transport barrier. They also showed that $\overline{E}_r$ can move the transport barrier outward and that the resulting particle confinement is further improved. The two diffusion coefficients, $D_{\rm ext}$ and $\overline{D}$, were found to always differ and, in the presence of the transport barrier, the difference became large. This difference was explained by using a one-dimensional diffusion equation and Dynkin's equation with a simple profile for the local diffusion coefficient, i.e. one in the form of a step function with a low value inside the transport barrier and a high value outside the barrier.

Acknowledgments

This work was supported by the Korea Advanced Institute of Science and Technology and the U.S. Department of Energy under contract No. DEFG03–96ER–54346. Computing resources were provided by the Texas Advanced Computing Center (TACC).

APPENDIX : MEAN EXIT TIME AND DYNKIN'S EQUATION

Dynkin's equation and its relationship to the mean exit time is well explained in several books on probability theory and stochastic differential equation [25,26]. Here we briefly summarize the salient points, which are needed for our problem.

The equation governing particles undergoing Brownian motion in a domain Ω is given by

$$\frac{d\boldsymbol{x}}{dt} = \boldsymbol{b}(\boldsymbol{x}) + \sigma(\boldsymbol{x})\boldsymbol{\xi}(t)\,, \tag{A1}$$

where $\boldsymbol{\xi}(t)$ is a random function of time that causes the Brownian motion and satisfies $\langle \xi_i(t)\xi_j(t')\rangle = \delta_{ij}\delta(t-t')$. The quantity $\mathbf{b}$ is deterministic. The particle density, n, obeys

$$\frac{\partial n(\boldsymbol{x})}{\partial t} = -\sum_i \frac{\partial}{\partial x_i}\left[b_i(\boldsymbol{x})n(\boldsymbol{x})\right] + \frac{1}{2}\sum_{i,j}\frac{\partial^2}{\partial x_i \partial x_j}\left[\left(\boldsymbol{\sigma}\boldsymbol{\sigma}^T\right)_{ij} n(\boldsymbol{x})\right]. \tag{A2}$$

which in our case where $\boldsymbol{b}(\boldsymbol{x}) = 0$, becomes a simple diffusion equation. We denote the first exit time of the particle that starts at $\boldsymbol{x}_0 \in \Omega$ at time $t = t_0$ as τ_{x_0,t_0}, and consider the solution of the following problem:

$$\frac{\partial u(\boldsymbol{x},t)}{\partial t} + \mathcal{M}u(\boldsymbol{x},t) = -1, \qquad t \geq t_0, \boldsymbol{x} \in \Omega, \tag{A3}$$

where $\mathcal{M}$ is the adjoint operator given by

$$\mathcal{M} = \boldsymbol{b}(\boldsymbol{x})\cdot\nabla + \frac{1}{2}\sum_{i,j}(\sigma\sigma^T)_{i,j}\frac{\partial^2}{\partial x_i \partial x_j}, \tag{A4}$$

and the boundary condition is $u(\boldsymbol{x},t) = 0$ for $\boldsymbol{x} \in \partial\Omega$. The differential of $u(\boldsymbol{x},t)$ is given by Ito's formula [25],

$$du(\boldsymbol{x},t) = \left(\frac{\partial u}{\partial t} + \mathcal{M}u\right)dt + \sum_{i,j}(\nabla u)_i^T\,\sigma_{i,j}\xi_j(t)dt, \tag{A5}$$

which leads to

$$u(\boldsymbol{x},t) = u(\boldsymbol{x}_0,t_0) + \int_{t_0}^{t}\left(\frac{\partial u}{\partial t} + \mathcal{M}u\right)dt' + \int_{t_0}^{t}(\nabla u)^T\cdot\sigma\cdot\boldsymbol{\xi}(t')dt' \tag{A6}$$

for $t_0 \leq t \leq \tau_{x_0,t_0}$. Setting $t = \tau_{x_0,t_0}$ and taking the average of both sides of Eq. (A6), we obtain

$$\langle u(\boldsymbol{x}, \tau_{x_0,t_0})\rangle = u(\boldsymbol{x}_0, t_0) + \langle \int_{t_0}^{\tau_{x_0,t_0}} (-1)dt' \rangle = u(\boldsymbol{x}_0, t_0) - \langle \tau_{x_0,t_0} \rangle + t_0. \tag{A7}$$

In the first identity, Eq. (A3) and $\langle \boldsymbol{\xi}(t) \rangle$ were used. Since $\boldsymbol{x}$ reaches $\partial\Omega$ at $t = \tau_{x_0,t_0}$ and u vanishes on $\partial\Omega$, the left hand side of Eq. (A7) is zero and we therefore obtain

$$\langle \tau_{x_0,t_0} \rangle = t_0 + u(\boldsymbol{x}_0, t_0). \tag{A8}$$

If we set $t_0 = 0$ and assume that a steady state is reached, then we have

$$\langle \tau_{x_0} \rangle = u(\boldsymbol{x}_0), \tag{A9}$$

where $u(x)$ is the solution of the following elliptic boundary value problem

$$\begin{aligned} \mathcal{M}u(x) &= -1 \quad \text{in } \Omega, \\ u(x) &= 0 \quad \text{on } \partial\Omega\,. \end{aligned} \tag{A10}$$

This equation is called Dynkin's equation. For our problem, we reduce this equation to one-dimension, in which case Eq. (A10) has the simple form

$$D(x)\frac{\partial^2 u(x)}{\partial x^2} = -1\,. \tag{A11}$$

REFERENCES

[1] F.M. Levinton, M.C. Zarnstorff, S.H. Batha, M. Bell, R.E. Bell, R.V. Budny, Z. Chang, E. Fredrickson, A. Janos, J. Manickam, A. Ramsey, S.A. Sabbagh, G.L. Schmidt, E.J. Synakowski, and G. Taylor, Phys. Rev. Lett. **75**, 4417 (1995).

[2] E. Mazzucato, S.H. Batha, M. Beer, M. Bell, R.E. Bell, R.V. Budny, C. Bush, T.S. Hahm, G.W. Hammett, F.M. Levinton, R. Nazikian, H. Park, G. Rewoldt, G.L. Schmidt, E.J. Synakowski, W.M. Tang, G. Taylor, and M.C. Zarnstorff, Phys. Rev. Lett. 77, 3145 (1996).

[3] F.X. Söldner, Yu.F. Baranov, D.V. Bartlett, C.D. Challis, H. Chen, I. Coffey, G.A. Cottrell, A. Ekedahl, C. Gormezano, C.M. Greenfield, G.T.A. Huysmans, E.A. Lazarus, X. Litaudon, T.C. Luce, B.W. Rice, V.V. Parail, F. Rochard, P. Schild, A.C.C. Sips, E.J. Strait, B.J.D. Tubbing, M.G. von Hellermann, M.R. Wade, D.J. Ward, Nucl. Fusion **39**, 407(1999).

[4] W. Horton, Rev. Mod. Phys. **71**, 735 (1999)

[5] W. Horton, H.-B. Park, J.-M. Kwon, D. Strozzi, P.J. Morrison, and D.-I. Choi, Phys. Plasmas **5**, 3910 (1998).

[6] D. del-Castillo-Negrete and P.J. Morrison, Phys. Fluids A **5**, 948 (1993).

[7] D. del-Castillo-Negrete, J.M. Greene, and P.J. Morrison, Physica D **91**, 1 (1996).

[8] D. del-Castillo-Negrete, J.M. Greene, and P.J. Morrison, Physica D **100**, 311 (1996).

[9] J.B. Taylor and H.R. Wilson, Plasma Phys. Controlled Fusion **38**, 1999 (1996).

[10] P. Zhu, W. Horton, and H. Sugama, Phys. Plasmas **6**, 2503 (1999).

[11] D.L. Brower, W.A. Peebles, N.C. Luhmann, Jr., and R.L. Savage, Jr., Phys. Rev. Lett. **54**, 689 (1985).

[12] E. Mazzucato and R. Nazikian, Phys. Rev. Lett. **71**, 1840 (1993).

[13] J.W. Connor and J.B. Taylor, Phys. Fluids **30**, 3180(1987).

[14] R.J. Hastie, K.W. Hesketh, and J.B. Taylor, Nucl. Fusion **19**, 1223 (1979).

[15] W. Horton, Duk-In Choi, and W.M. Tang, Phys. Fluids **24**, 1077 (1981).

[16] J.W. Connor, J.B. Taylor, and H.R. Wilson, Phys. Rev. Lett. **70**, 1803 (1993).

[17] F. Romanelli and F. Zonca, Phys. Fluids **B5**, 4081 (1993).

[18] J.B. Taylor, H.R. Wilson, and J.W. Connor, Plasma Phys. Controlled Fusion **38**, 243 (1996).

[19] A.D. Beklemishev and W. Horton, Phys. Fluids B **4**, 200 (1992).

[20] J.Y. Kim, Y. Kishimoto, M. Wakatani, and T. Tajima, Phys. Plasmas **3**, 3689 (1996).

[21] D.R. Ernst, M.G. Bell, R.E. Bell, C.E. Bush, Z. Chang, E. Fredrickson, L.R. Grisham, K.W. Hill, D.L. Jassby, D.K. Mansfield, D.C. McCune, H.K. Park, A.T. Ramsey, S.D. Scott, J.D. Strachan, E.J. Synakowski, G. Taylor, M. Thompson, and R.M. Wieland, Phys. Plasmas **5**, 665 (1998).

[22] M. Ottaviani, W. Horton, and M. Erba, Plasma Phys. Controlled Fusion **39**, 1461 (1997).

[23] H.-B. Park, E.-G. Heo, W. Horton, and D.-I. Choi, Phys. Plasmas **4**, 3273 (1997).

[24] P.C. Efthimion, S. von Goeler, W.A. Houlberg, E.J. Synakowski, M.C. Zarnstorff, S.H. Batha, R.E. Bell, M. Bitter, C.E. Bush, F.M. Levinton, E. Mazzucato, D.McCune, D. Mueller, H. Park, A.T. Ramsey, A.L. Roquemore, and G. Taylor, Phys. Plasmas **5**, 1832(1998).

[25] C.W. Gardiner, *Handbook of Stochastic Methods* (Springer, New York, 1983).

[26] Zeev Schuss, *Theory and Applications of Stochastic Differential Equations* (Wiley, New York, 1980).

TABLE CAPTIONS

Table 1 D_{ext} and $\overline{D}$ for three confinement cases. The values in parenthesis are cases where $\overline{E}_r$ is included.

FIGURE CAPTIONS

Fig.1 Radial profiles of q, T_i, T_e, and n_i for three confinement cases. Case I models an L-mode TFTR plasma, Case II models the ERS TFTR plasma, and Case III models the JET optimized shear plasma.

Fig.2 Radial profiles of the equilibrium radial electric field, $\overline{E}_r$, for Case II and Case III.

Fig.3 The coupling element $|\alpha V/\kappa|^{1/2}$ of Eq. (29) for different toroidal modes, $L = 20, 22, 25$, for Case I, the L-mode plasma.

Fig.4 The coupling element $|\alpha V/\kappa|^{1/2}$ of Eq. (29) for different toroidal modes, $L = 20, 22, 25$, for Case II, the ERS plasma. Triangles represent the case with $\overline{E}_r$ and squares represent the case without $\overline{E}_r$.

Fig.5 The coupling element $|\alpha V/\kappa|^{1/2}$ of Eq. (29) for different toroidal modes, $L = 20, 22, 25$, for Case III, the OS plasma. Triangles represent the case with $\overline{E}_r$ and squares represent the case without $\overline{E}_r$.

Fig.6 Particle fluxes at two different positions $r = 0.4a$ and $r = 0.95a$ for Case I.

Fig.7 Time series of the running diffusion coefficient $D(t)$ and the mean exit time $\langle \tau_{\text{ext}} \rangle$ for Case I.

Fig.8 Particle fluxes at two different positions $r = 0.4a$ and $r = 0.95a$ for Case II. The solid line represents the case with $\overline{E}_r$ and the square dotted line represents the case without $\overline{E}_r$.

Fig.9 Time series of the running diffusion coefficient $D(t)$ and the mean exit time $\langle \tau_{\text{ext}} \rangle$ for Case II. The solid line represents the case with $\overline{E}_r$ and the square dotted line represents the case without $\overline{E}_r$.

Fig.10 Particle fluxes at two different positions $r = 0.4a$ and $r = 0.95a$ for Case III. The solid line represents the case with $\overline{E}_r$ and the square dotted line represents the case without $\overline{E}_r$.

Fig.11 Time series of the running diffusion coefficient $D(t)$ and the mean exit time $\langle \tau_{\rm ext} \rangle$ for Case III. The solid line represents the case with $\overline{E}_r$ and the square dotted line represents the case without $\overline{E}_r$.

Fig.12 Radial profiles of the steady state particle density for three different cases. The profiles are normalized so that total particle number is the same. In (b) and (c), solid lines represent cases with $\overline{E}_r$ and the square dotted lines represent cases without $\overline{E}_r$.

TABLE I. D_{ext} and $\overline{D}$ for three confinement cases. The values in parenthesis are cases where $\overline{E}_r$ is included.

	$\overline{D}$ (cm^2/s)	D_{ext} (cm^2/s)
Case I	8.35×10^4	1.52×10^5
Case II	2.75×10^4 (1.81×10^4)	1.92×10^5 (1.36×10^5)
Case III	1.39×10^5 (5.94×10^4)	4.81×10^5 (1.30×10^5)

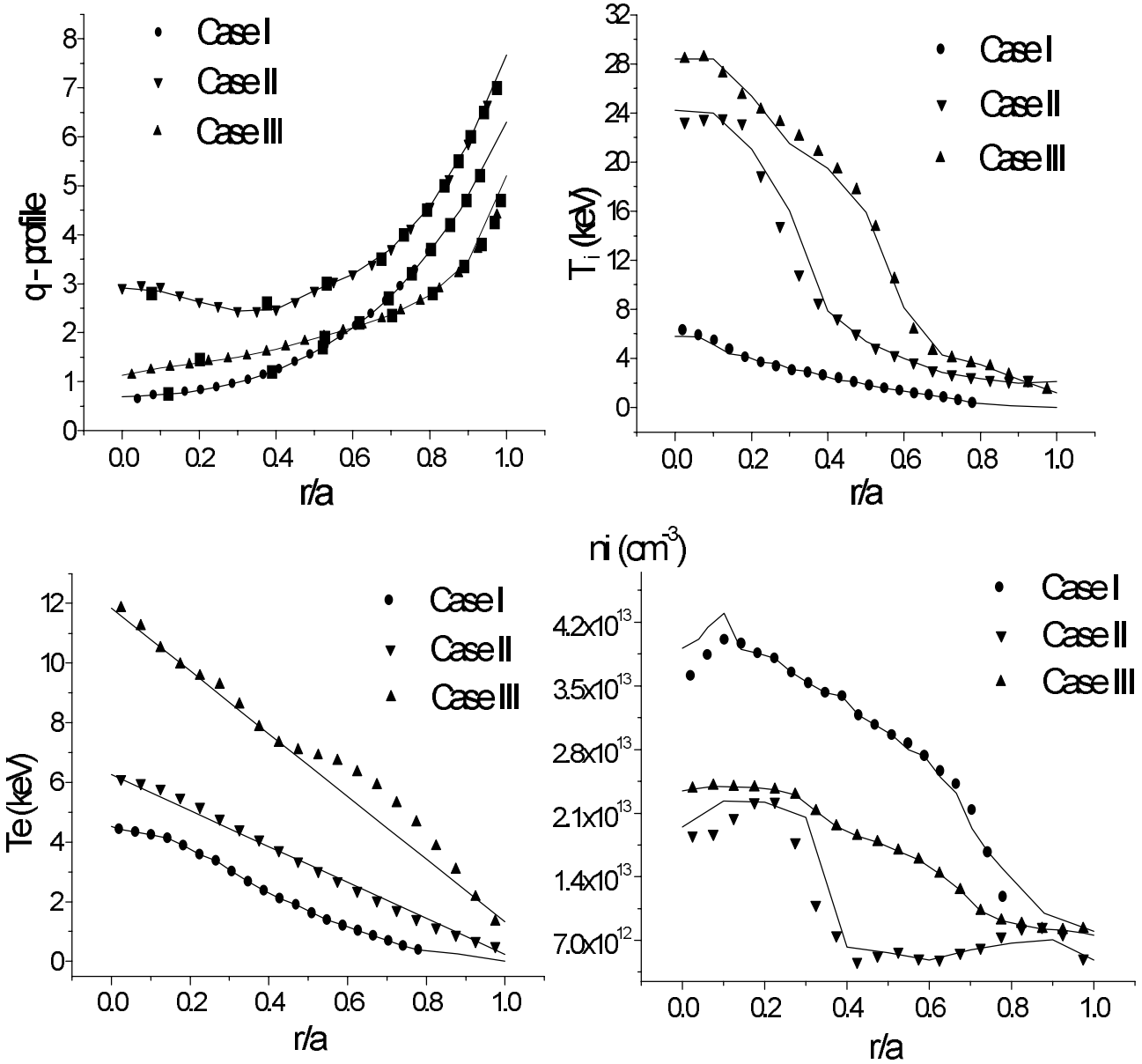
Case I
Case II
Case III
q - profile
r/a
Ti (keV)
Te (keV)
ni (cm-3)
4.2x10^13
3.5x10^13
2.8x10^13
2.1x10^13
1.4x10^13
7.0x10^12

Fig. 1

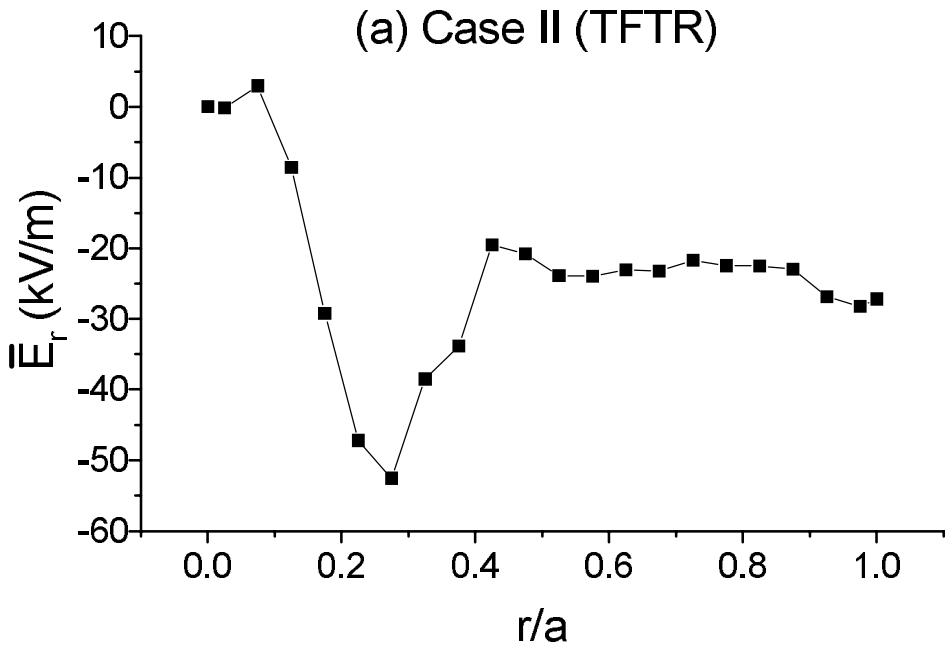
(a) Case II (TFTR)
10
0
-10
-20
-30
-40
-50
-60
$\bar{E}_r$ (kV/m)
0.0
0.2
0.4
0.6
0.8
1.0
r/a

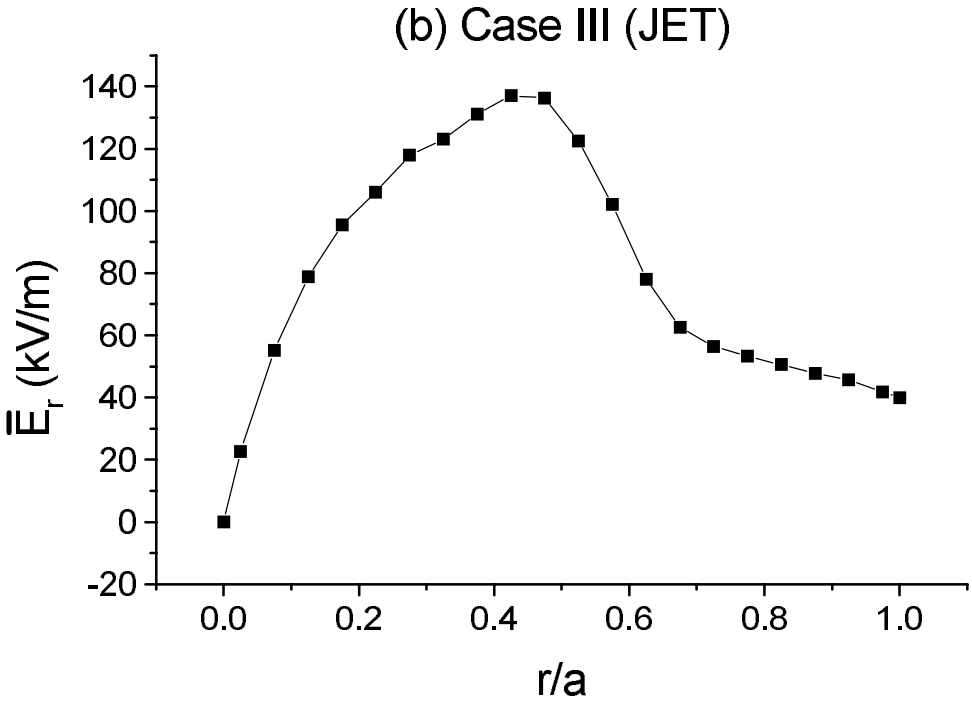
(b) Case III (JET)
140
120
100
80
60
40
20
0
-20
$\bar{E}_r$ (kV/m)
0.0
0.2
0.4
0.6
0.8
1.0
r/a

Fig. 2

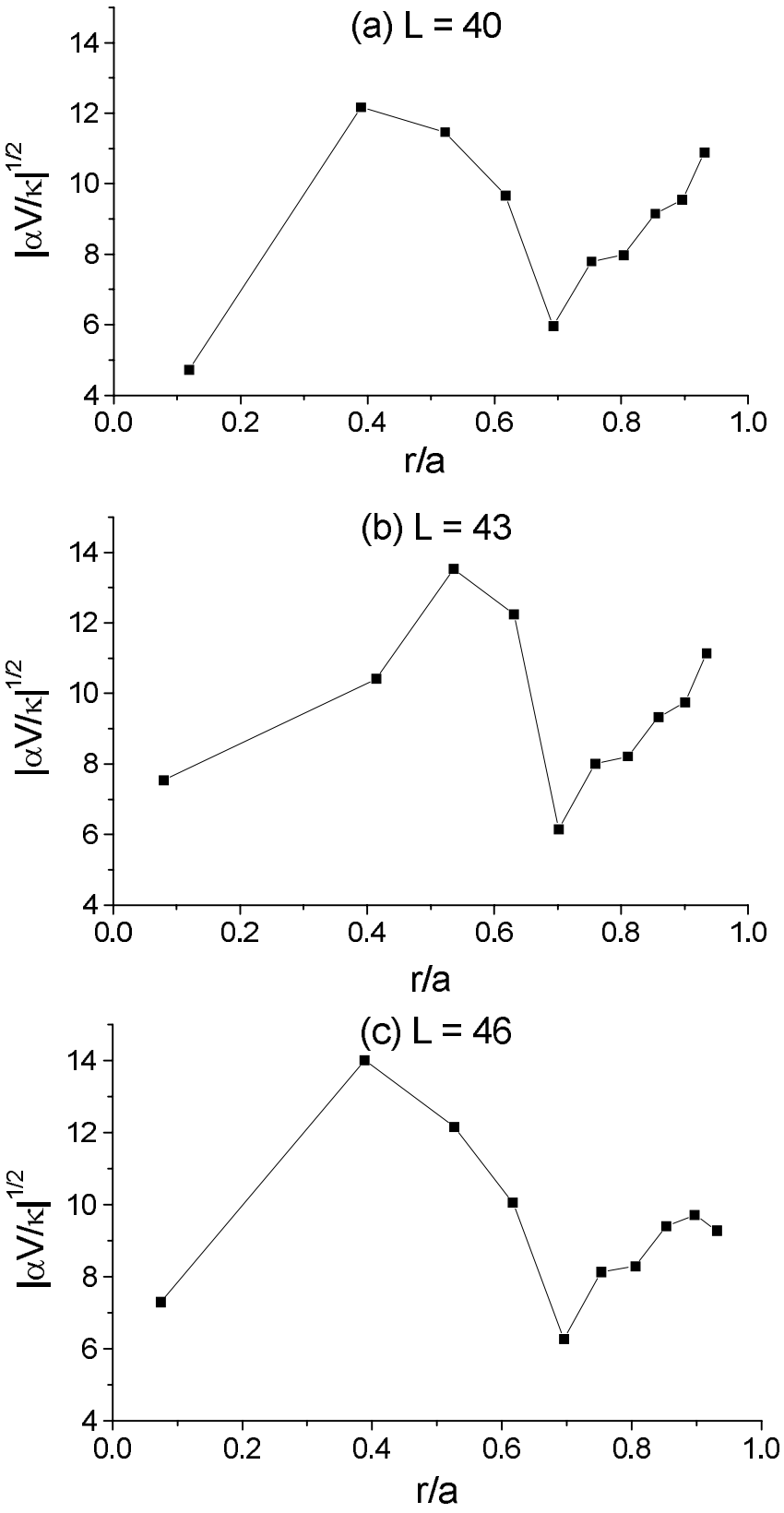

Fig. 3

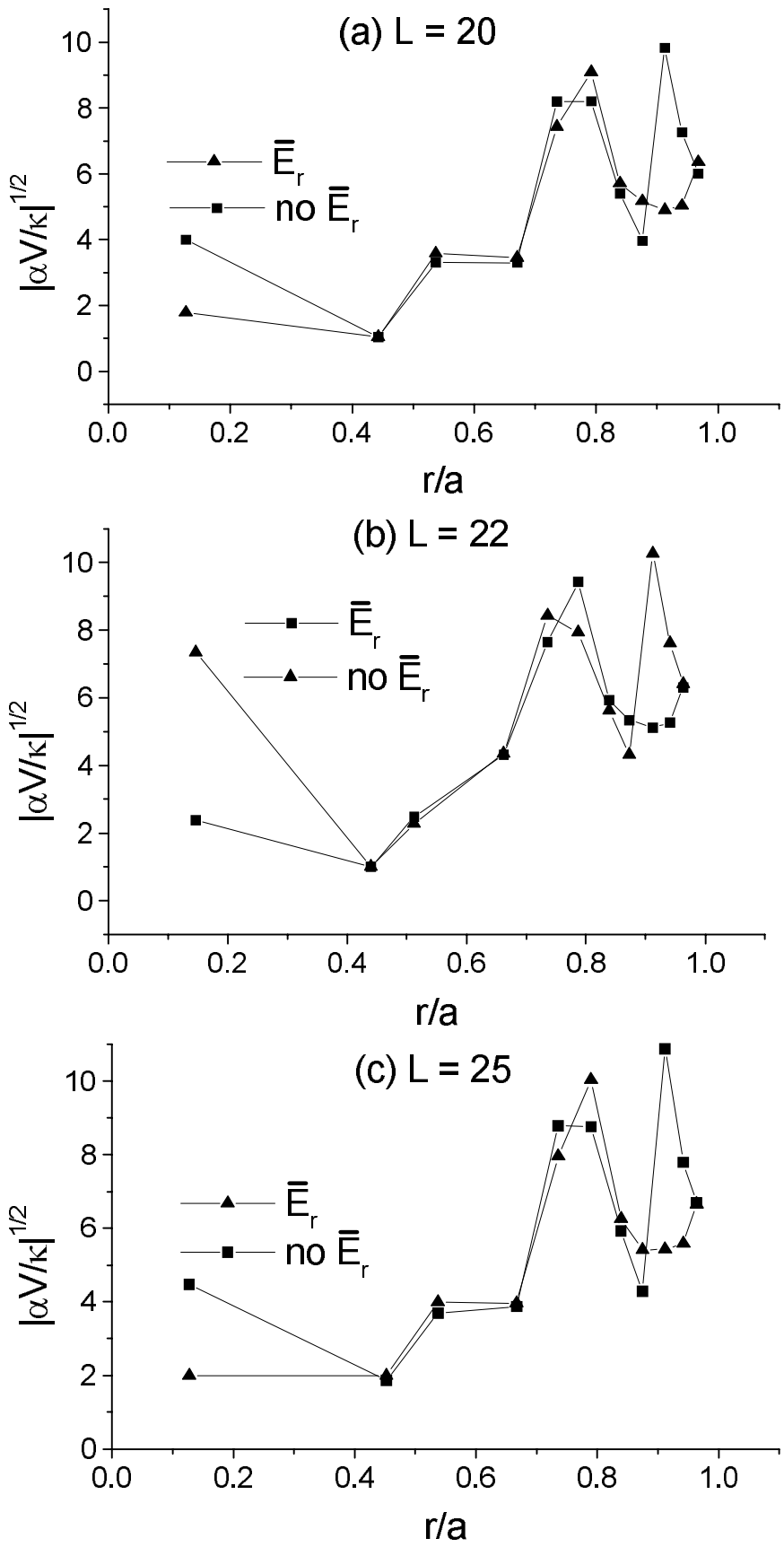
(a) L = 20
$\bar{\bar{E}}_r$
no $\bar{\bar{E}}_r$
$|\alpha V/\kappa|^{1/2}$
r/a
(b) L = 22
$\bar{\bar{E}}_r$
no $\bar{\bar{E}}_r$
$|\alpha V/\kappa|^{1/2}$
r/a
(c) L = 25
$\bar{\bar{E}}_r$
no $\bar{\bar{E}}_r$
$|\alpha V/\kappa|^{1/2}$
r/a

Fig. 4

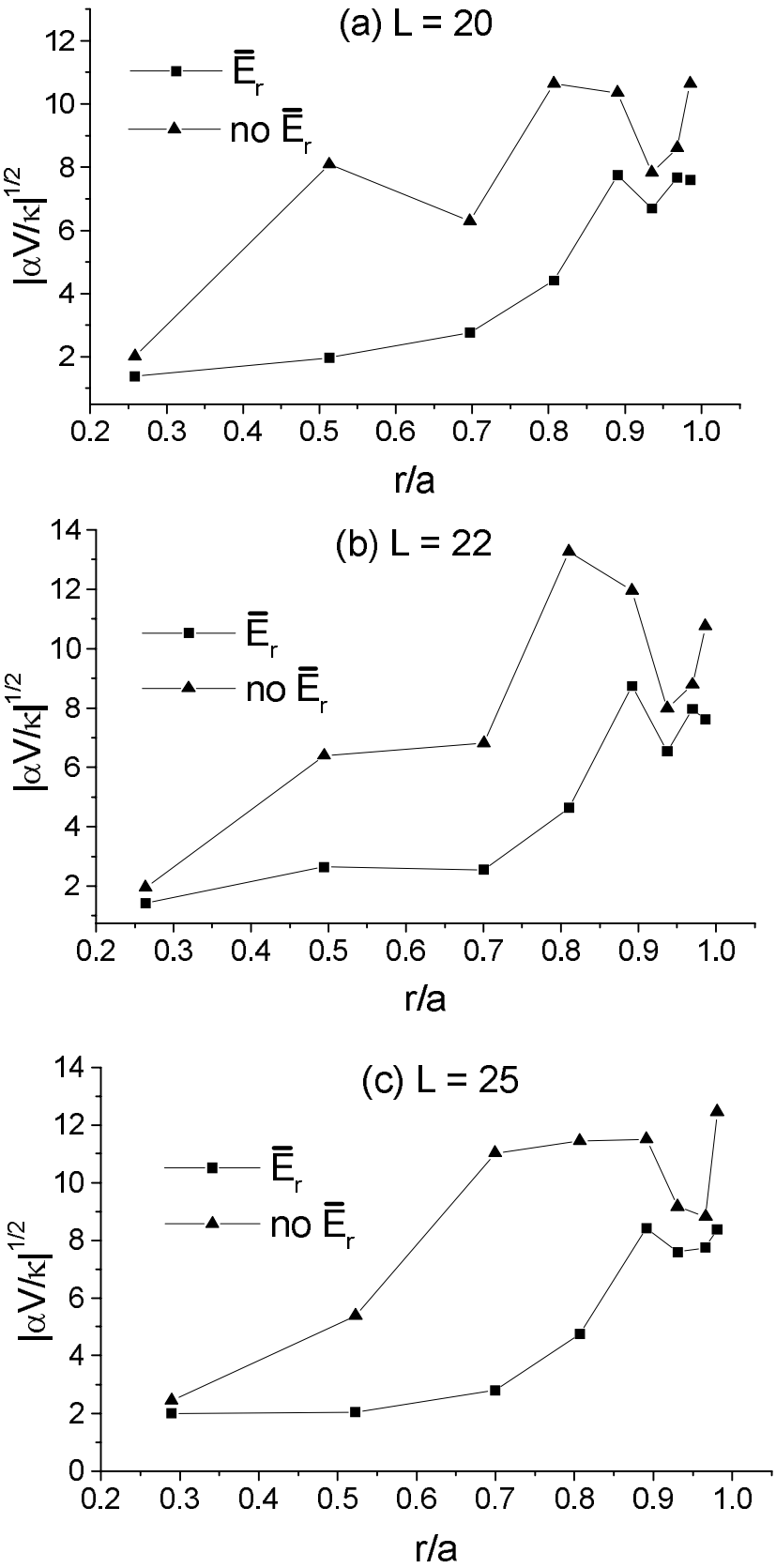
(a) L = 20
$\bar{E}_r$
no $\bar{E}_r$
$|\alpha V/\kappa|^{1/2}$
r/a
(b) L = 22
$\bar{E}_r$
no $\bar{E}_r$
$|\alpha V/\kappa|^{1/2}$
r/a
(c) L = 25
$\bar{E}_r$
no $\bar{E}_r$
$|\alpha V/\kappa|^{1/2}$
r/a

Fig. 5

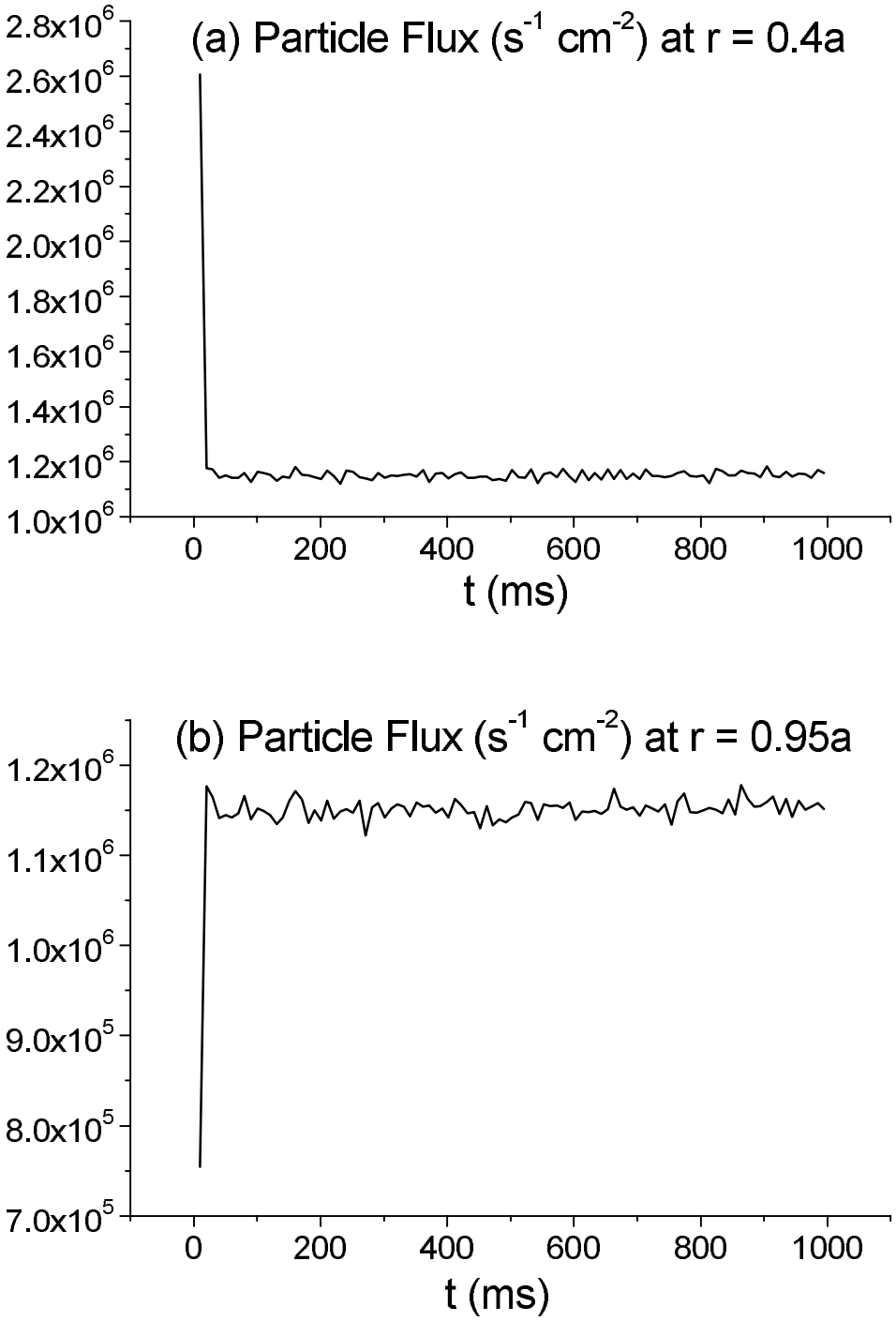
(a) Particle Flux (s-1 cm-2) at r = 0.4a
2.8x10^6
2.6x10^6
2.4x10^6
2.2x10^6
2.0x10^6
1.8x10^6
1.6x10^6
1.4x10^6
1.2x10^6
1.0x10^6
0
200
400
600
800
1000
t (ms)
(b) Particle Flux (s-1 cm-2) at r = 0.95a
1.2x10^6
1.1x10^6
1.0x10^6
9.0x10^5
8.0x10^5
7.0x10^5
0
200
400
600
800
1000
t (ms)

Fig. 6

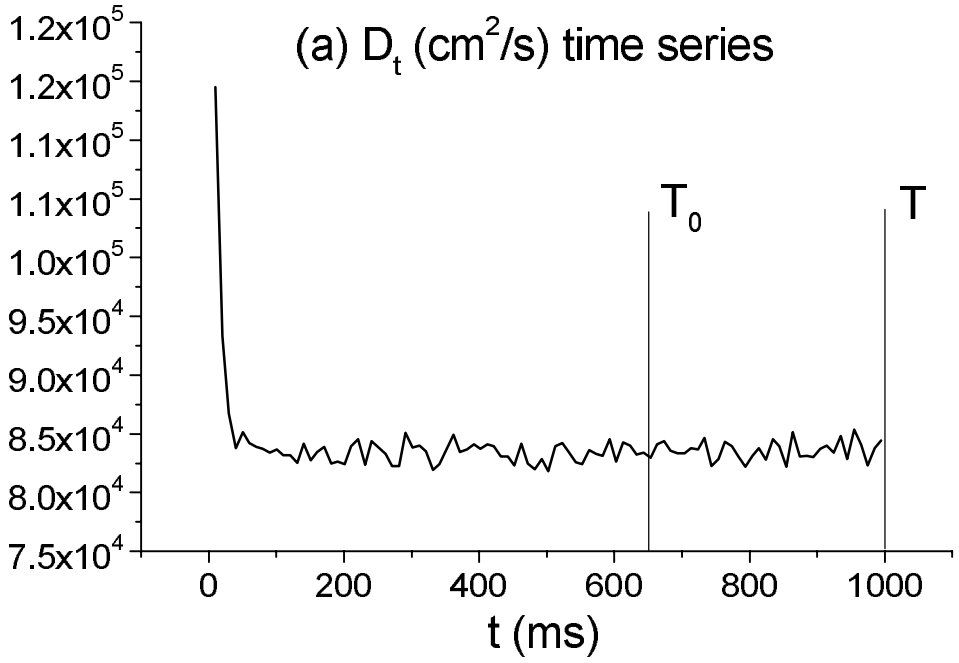
(a) D_t (cm^2/s) time series
1.2x10^5
1.2x10^5
1.1x10^5
1.1x10^5
1.0x10^5
9.5x10^4
9.0x10^4
8.5x10^4
8.0x10^4
7.5x10^4
T_0
T
0
200
400
600
800
1000
t (ms)

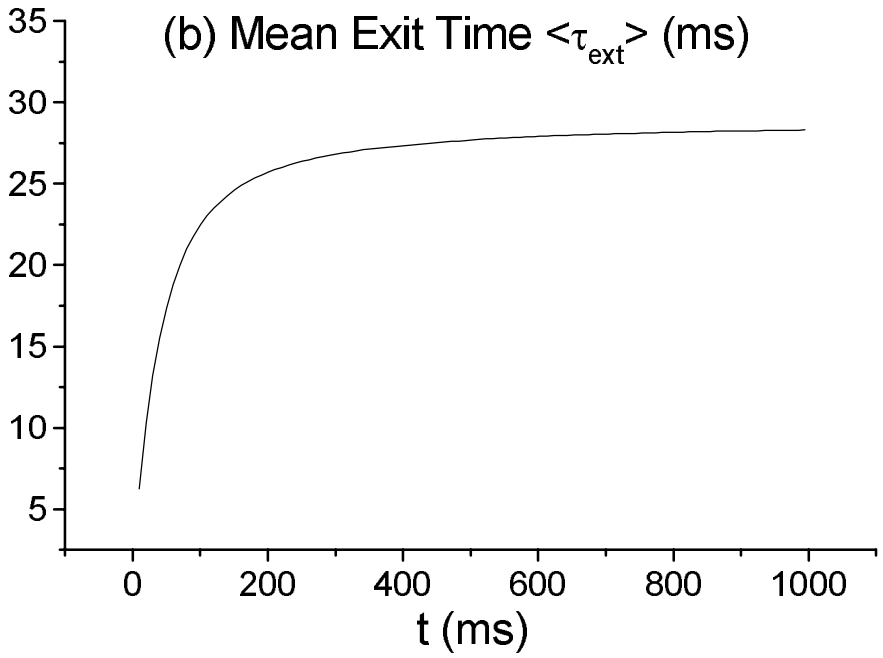
(b) Mean Exit Time $<\tau_{ext}>$ (ms)
35
30
25
20
15
10
5
0
200
400
600
800
1000
t (ms)

Fig. 7

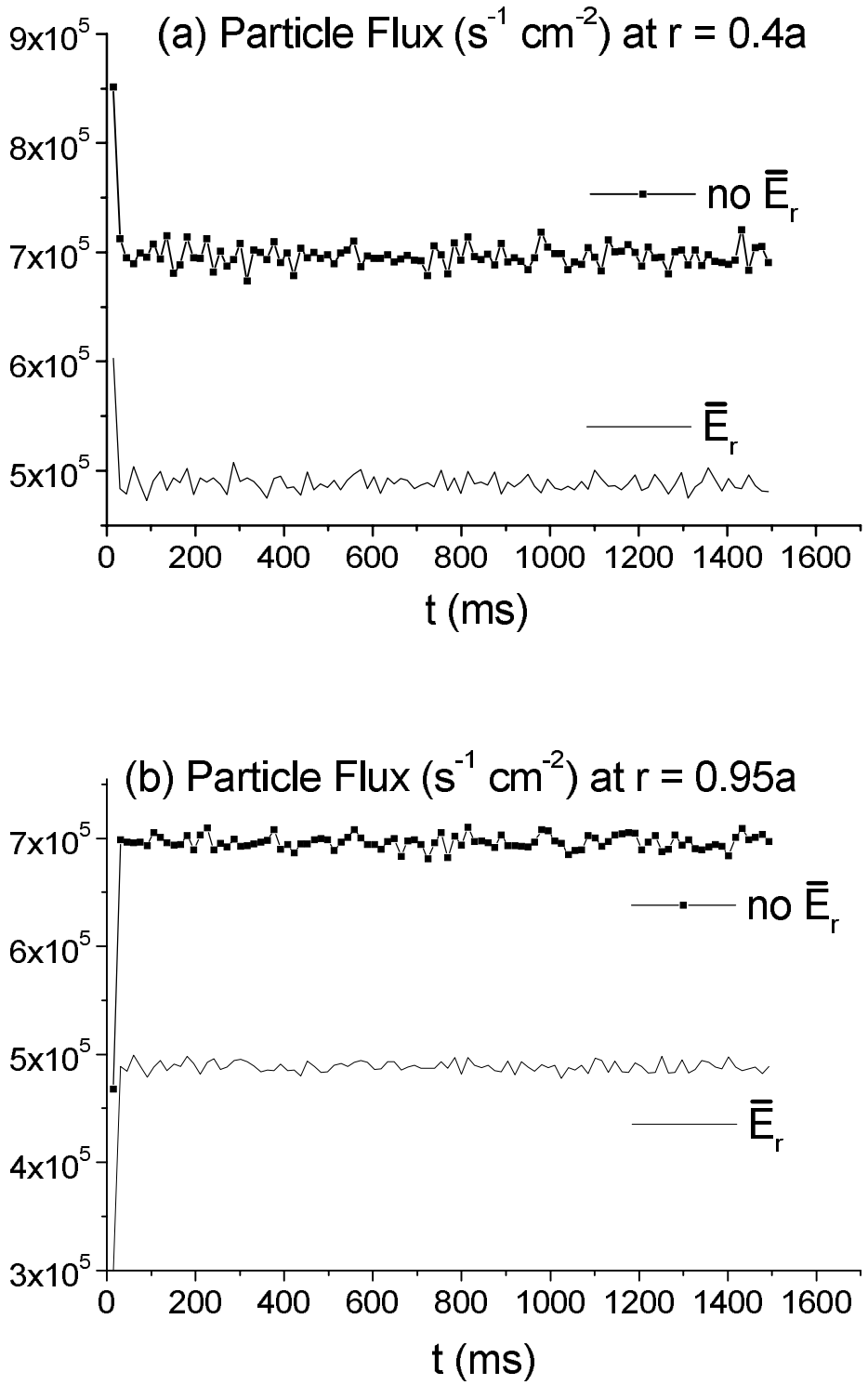
(a) Particle Flux (s-1 cm-2) at r = 0.4a
9x10^5
8x10^5
7x10^5
6x10^5
5x10^5
no Ēr
Ēr
0
200
400
600
800
1000
1200
1400
1600
t (ms)
(b) Particle Flux (s-1 cm-2) at r = 0.95a
7x10^5
6x10^5
5x10^5
4x10^5
3x10^5
no Ēr
Ēr
0
200
400
600
800
1000
1200
1400
1600
t (ms)

Fig. 8

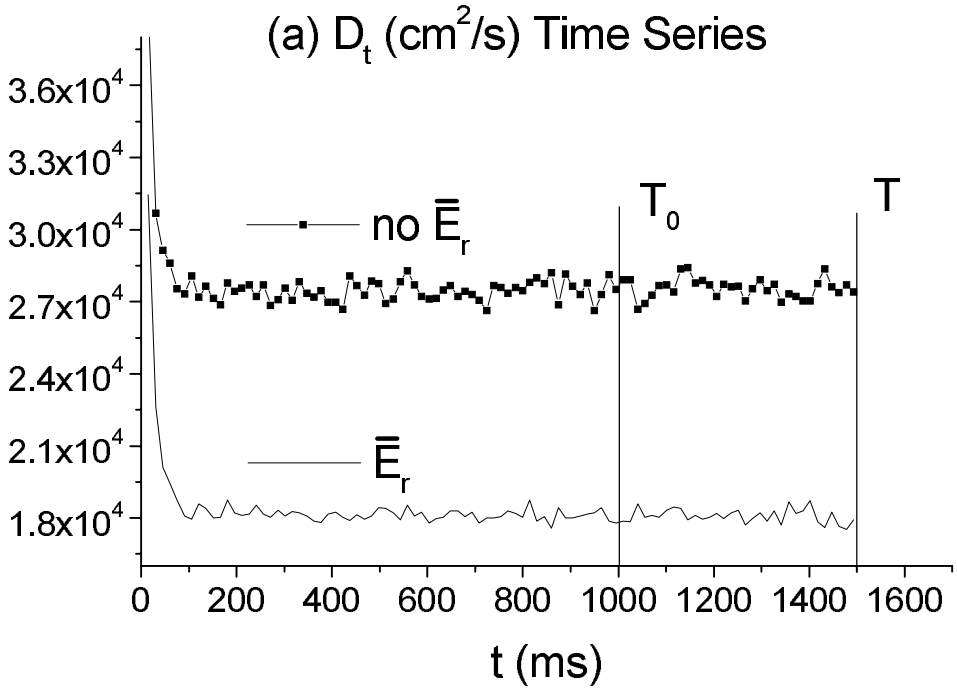
(a) D_t (cm^2/s) Time Series
3.6x10^4
3.3x10^4
3.0x10^4
2.7x10^4
2.4x10^4
2.1x10^4
1.8x10^4
no $\bar{E}_r$
$\bar{E}_r$
T_0
T
0
200
400
600
800
1000
1200
1400
1600
t (ms)

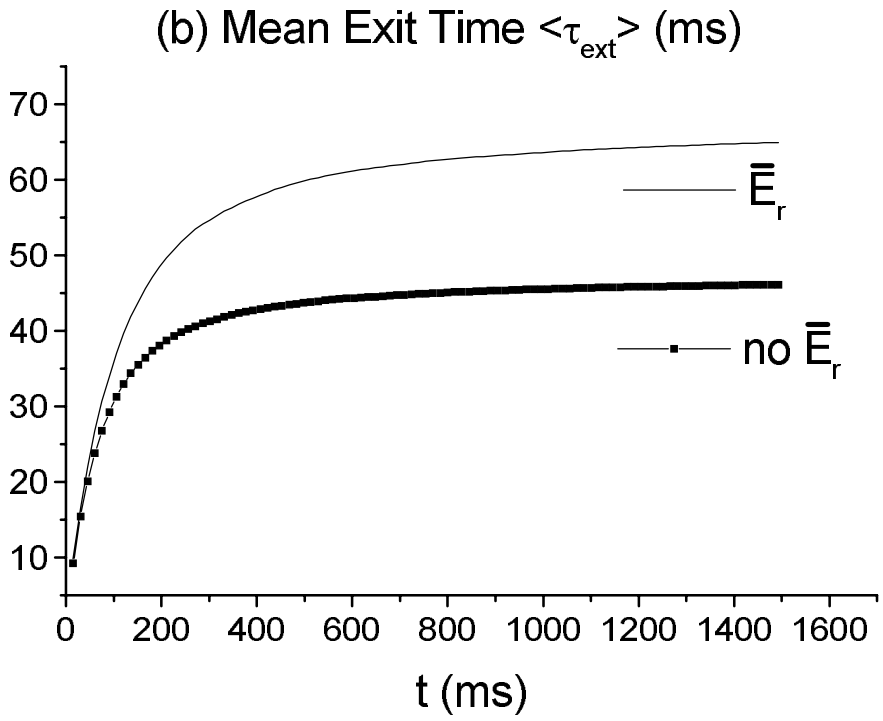
(b) Mean Exit Time <τ_{ext}> (ms)
70
60
50
40
30
20
10
$\bar{E}_r$
no $\bar{E}_r$
0
200
400
600
800
1000
1200
1400
1600
t (ms)

Fig. 9

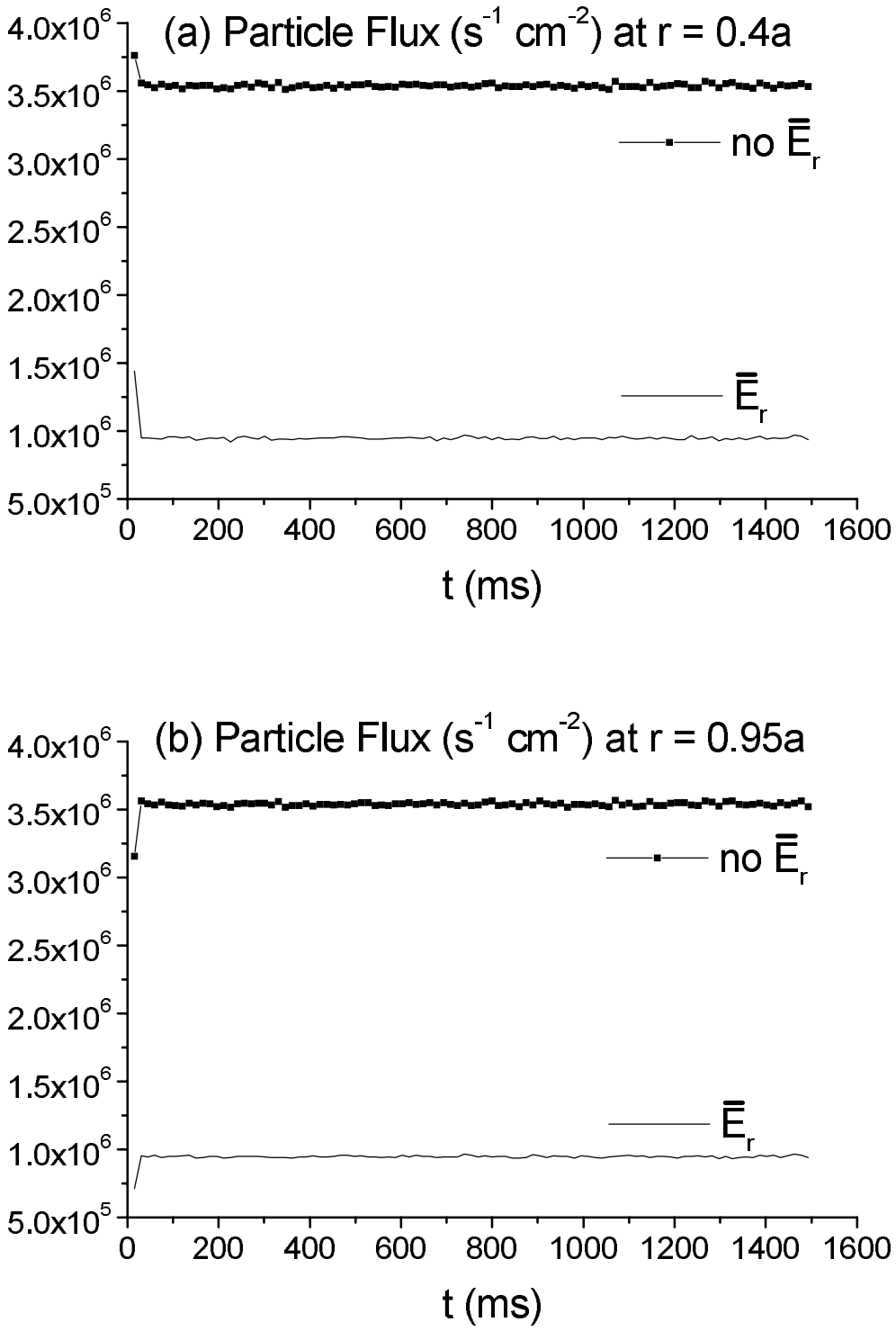
(a) Particle Flux (s-1 cm-2) at r = 0.4a
4.0x10^6
3.5x10^6
3.0x10^6
2.5x10^6
2.0x10^6
1.5x10^6
1.0x10^6
5.0x10^5
no Ē_r
Ē_r
0
200
400
600
800
1000
1200
1400
1600
t (ms)
(b) Particle Flux (s-1 cm-2) at r = 0.95a
4.0x10^6
3.5x10^6
3.0x10^6
2.5x10^6
2.0x10^6
1.5x10^6
1.0x10^6
5.0x10^5
no Ē_r
Ē_r
0
200
400
600
800
1000
1200
1400
1600
t (ms)

Fig. 10

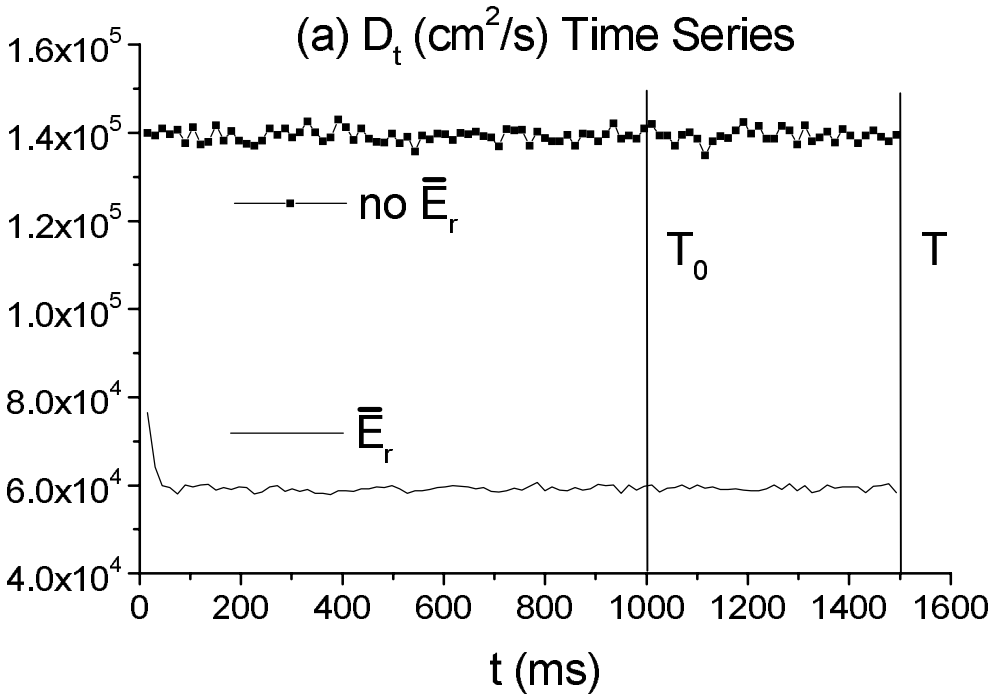
(a) D_t (cm^2/s) Time Series
1.6x10^5
1.4x10^5
1.2x10^5
1.0x10^5
8.0x10^4
6.0x10^4
4.0x10^4
no $\bar{\bar{E}}_r$
$\bar{\bar{E}}_r$
T_0
T
0
200
400
600
800
1000
1200
1400
1600
t (ms)

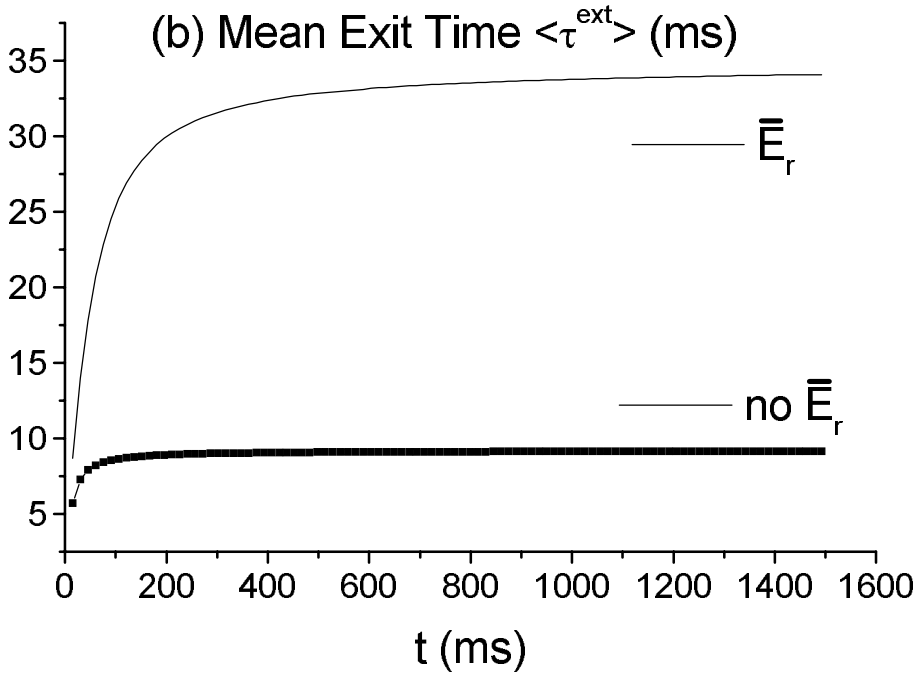
(b) Mean Exit Time $<\tau^{ext}>$ (ms)
35
30
25
20
15
10
5
$\bar{\bar{E}}_r$
no $\bar{\bar{E}}_r$
0
200
400
600
800
1000
1200
1400
1600
t (ms)

Fig. 11

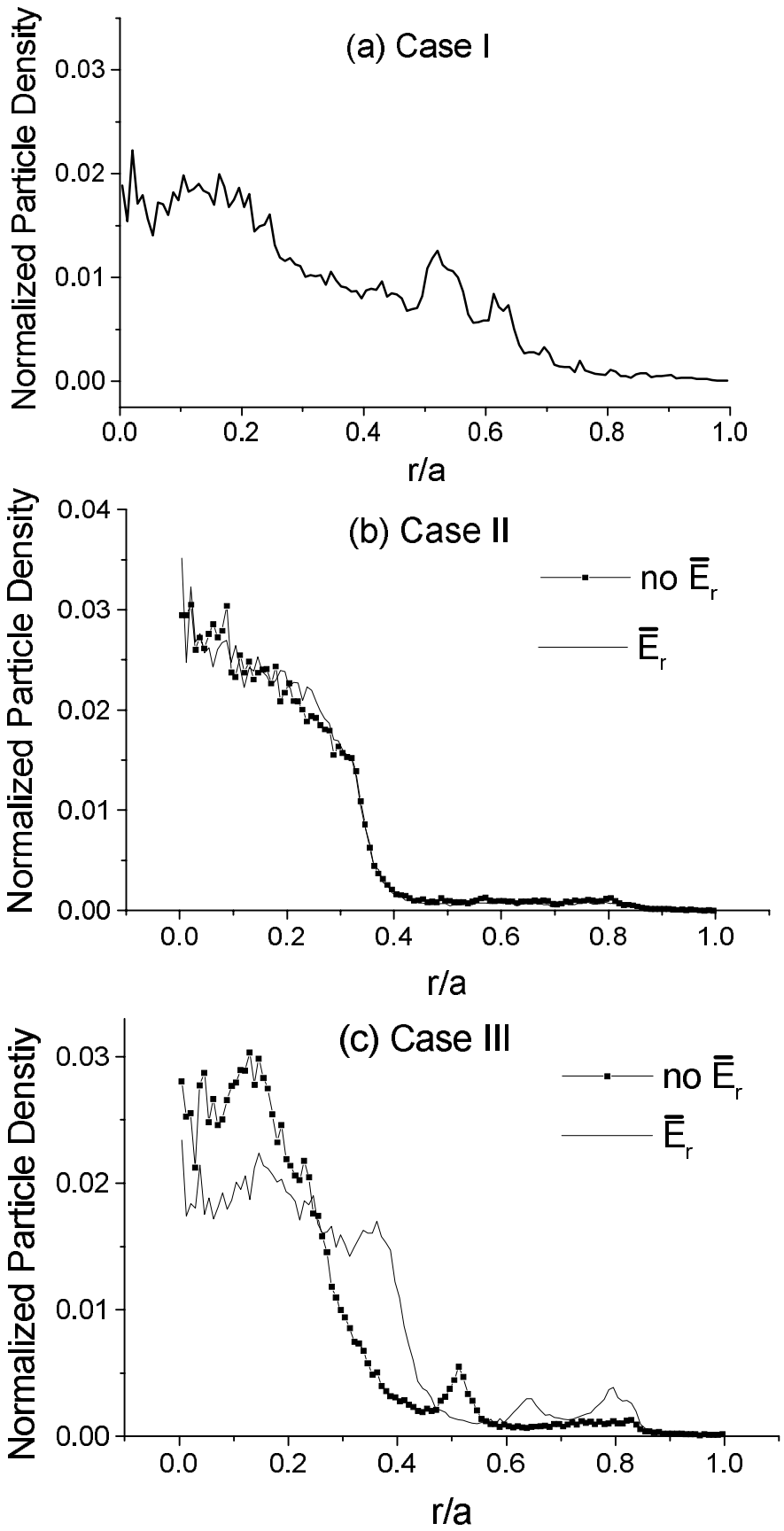
(a) Case I
Normalized Particle Density
0.03
0.02
0.01
0.00
0.0
0.2
0.4
0.6
0.8
1.0
r/a
(b) Case II
Normalized Particle Density
0.04
0.03
0.02
0.01
0.00
no $\bar{E}_r$
$\bar{E}_r$
r/a
(c) Case III
Normalized Particle Denstiy
0.03
0.02
0.01
0.00
no $\bar{E}_r$
$\bar{E}_r$
r/a

Fig. 12